New Verbeekite-type polymorphic phase and rich phase diagram in the $PdSe_{2-x}Te_x$ system

Wenhao Liu,[1] Mehrdad Rostami Osanloo,[1] Xiqu Wang,[3] Sheng Li,[1] Nikhil Dhale,[1] Hanlin Wu,[1] Maarten L. Van de Put,[2] Sabyasachi Tiwari,[2] William G. Vandenberghe,[2] and Bing Lv[1,2,*]

[1]*Department of Physics, University of Texas at Dallas, Richardson, Texas 75080, USA*

[2]*Department of Materials Science and Engineering, University of Texas at Dallas, Richardson, Texas 75080, USA*

[3]*Department of Chemistry, University of Houston, Houston, Texas 77004, USA*

(Received 19 March 2021; revised 29 June 2021; accepted 6 July 2021; published 22 July 2021)

We report a combined experimental and theoretical study of the $PdSe_{2-x}Te_x$ system. With increasing Te fraction, structural evolutions, first from an orthorhombic phase (space group *Pbca*) to a monoclinic phase (space group $C2/c$) and then to a trigonal phase (space group $P\text{-}3m1$), are observed accompanied with clearly distinct electrical transport behavior. The new monoclinic phase ($C2/c$) belongs to the very rare Verbeekite polymorphism and is discovered within a narrow range of Te composition ($0.3 \leqslant x \leqslant 0.8$). Electronic calculations and detailed transport analysis of the Verbeekite polymorphic $PdSe_{1.3}Te_{0.7}$ phase are presented. In the trigonal phase region, superconductivity with enhanced critical temperature is also observed within a narrow range of Te content ($1.0 \leqslant x \leqslant 1.2$). The rich phase diagram, new polymorphic structure, and abnormally enhanced superconductivity could further stimulate interest to explore new types of polymorphs and investigate their transport and electronic properties in the family of transition metal dichalcogenides, which are of significant interest.

DOI: 10.1103/PhysRevB.104.024507

I. INTRODUCTION

The study of a variety of polymorphic structures of transition metal dichalcogenides (TMDs), and the discoveries of their unique properties through atomic-scale structure control, have emerged as a research frontier of science for new exciting physics as well as miniaturizing of electronic devices, energy conversion, and storage [1–9]. TMD polymorphs are chemically rather simple and structured with fundamental MX_2 layers, where M is a transition metal (such as V, Nb, Ta, Ti, Zr, Hf, Mo, W, Pd, and Pt) and X is a chalcogen atom (such as S, Se, or Te) [10]. With strong in-plane bonding and weak out-of-plane van der Waals interactions, these materials can be easily exfoliated down to atomic thickness and thus enable bottom-up atomic-scale structure control and unique stacking or twisting to reveal new physics or novel functionalities [11–13].

Research into various structures of TMDs has a long and fruitful history. Various polymorphic structures appear starting from either the trigonal prismatic or the octahedral coordination of the metal atoms. Depending on the different stacking order of atomic planes and possible distortions, the most commonly encountered arrangements are 1T (T, trigonal), 2H (H, hexagonal), 3R (R, rhombohedral), 1T′ (distorted 1T into monoclinic phase), and T_d (distorted 1T into orthorhombic phase) [14–18]. The digits (1–3) indicate the number of layers in the stacking sequence in the primitive unit cell.

The different polymorphs in TMDs often display drastically different physical phenomena. For example, three different polymorphs showing distinct properties are found for the $MoTe_2$ phases: 2H-$MoTe_2$ shows semiconducting behaviors with a band gap of about 1.1 eV, 1T′-$MoTe_2$ has a metallic behavior [19,20], and T_d-$MoTe_2$ is topologically nontrivial and a candidate Weyl semimetal [21,22]. Another example is found in the $TaSe_{2-x}Te_x$ system, where various polymorphic structures have been observed. With increasing Te concentration, the material appears as an incommensurate charge-density-wave (ICDW) 2H-$TaSe_2$ phase, as a 3R phase with a maximal superconducting transition temperature (T_c) of 2.4K, as a different 1T phase (also superconducting with lower T_c at 0.5–0.7 K), and finally as a normal metallic monoclinic $TaTe_2$ phase [23].

Interestingly, PdS_2 and $PdSe_2$, less studied TMDs [24–26], have a puckered pentagonal configuration with orthorhombic space group *Pbca* shown in Fig. 1(a). The *Pbca* space group is rarely found in TMDs and hosts pentagons. Pentagons are often considered as topological defects or geometrical frustrations [27]. Pentagonal graphene and SnS_2 have been theoretically predicted to possess quite unique physical properties, such as unusual negative Poisson's ratio or a room-temperature quantum spin Hall insulator state [28,29]. Different from the other TMDs where the metal coordination is either trigonal prismatic or octahedral (sometimes distorted), the Pd metal configuration in PdS_2 and $PdSe_2$ is in fact a rectangular net. $PdSe_2$ is highly stable in air down to the monolayer limit [30]. The band gap varies greatly from 0.5 eV in the bulk to 1.37 eV in monolayers, and the thin $PdSe_2$ field-effect transistors exhibit intrinsic ambipolar characteristic and high electron mobility [31,32]. Under high pressure, bulk $PdSe_2$ transforms from a pentagonal layered structure to a pyrite-type structure, and superconductivity up to 13.1 K emerges, which is the highest critical temperature

*blv@utdallas.edu

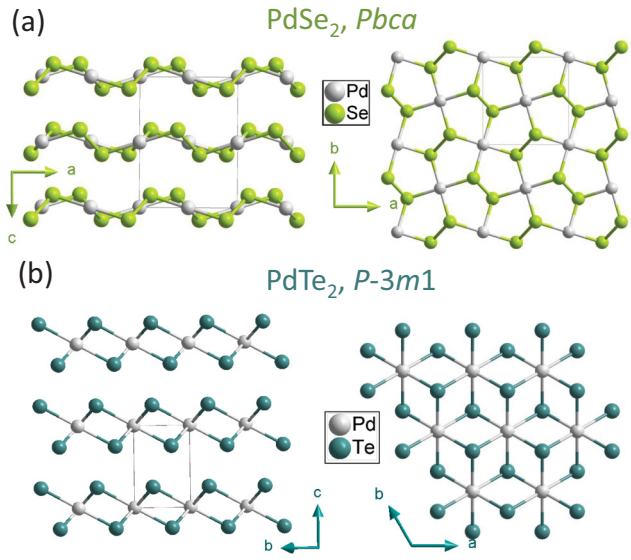

FIG. 1. Ball-and-stick models of (a) $PdSe_2$ and (b) $PdTe_2$ side view (left) and top view (right).

T_c among all the TMD materials to date [33]. On the other hand, $PdTe_2$ adopts the layered 1T structure with space group $P\text{-}3m1$ [Fig. 1(b)]. $PdTe_2$ has an octahedral (i.e., trigonal antiprismatic) coordination, is metallic, and is characterized by an ABC Se-Pd-Se stacking order within the layer. A Dirac semimetal and superconductivity with T_c of 1.65 K have been experimentally verified to coexist in $PdTe_2$ [34–36].

The distinct difference in structure and electronic properties of $PdSe_2$ and $PdTe_2$ motivate us to explore the possible structural evolution or transformation and their associated electrical transport behavior changes in the $PdSe_{2-x}Te_x$ system. We have demonstrated previously that the superconductivity of $PdTe_2$ can be enhanced up to 2.73 K when half of the Te in $PdTe_2$ is replaced by Se atoms [37]. Here, we study the full range of the $PdSe_{2-x}Te_x$ ($0 \leqslant x \leqslant 2$) system and discover a new $C2/c$ polymorphic structure analog to the high-pressure $PdSe_2$ Verbeekite phase [38,39]. We complement our experimental results with theoretical first-principles calculations. The $PdSe_2$-$PdTe_2$ phase diagram and associated electrical transport results, including superconductivity, are presented.

II. EXPERIMENTAL DETAILS

The $PdSe_{2-x}Te_x$ crystals were synthesized using self-flux methods. Pd ingots (99.95%, Alfa Aesar), Se shots (99.999%, Alfa Aesar), and Te pieces (99.999%, Alfa Aesar) were mixed in the right stoichiometric doping ratio in an Ar glove box with a total moisture and oxygen level less than 0.1 ppm. The source elements were loaded inside a silica tube, which was then flame sealed under vacuum and placed in a box furnace. The temperature was slowly increased to 800 °C, which was held for 3 days and followed by furnace cooling down to room temperature.

The chemical composition of the yield crystals was verified by energy-dispersive x-ray spectroscopy (EDX) on a DM07 Zeiss Supra 40 scanning electron microscope. Powder x-ray diffraction (XRD) measurements were carried out at room temperature on crushed crystals using a Rigaku SmartLab x-ray diffractometer equipped with Cu-K α radiation. Rietveld refinement was carried out using GSAS-II [40]. Resistivity was measured using the four-probe method in a Quantum Design Physical Property Measurement System (PPMS) down to 1.8 K. Four gold wires (30 μm in diameter) were pasted on the sample surface by silver epoxy as four probes.

The crystal structure of the new $PdSe_{1.2}Te_{0.8}$ phase was determined with single-crystal x-ray data measured on a Bruker SMART diffractometer equipped with an Apex II area detector and an Oxford Cryosystems 700 Series temperature controller with a Mo $K\alpha$ source ($\lambda = 0.710\,73$ Å). The collected data set was integrated using the Bruker Apex-II program, with the intensities corrected for the Lorentz factor, polarization, air absorption, and absorption due to variation in the path length through the detector faceplate. The data were scaled, and absorption correction was applied using SADABS. The structure was solved by using the intrinsic phasing method in SHELXT and refined using SHELXL with all atoms refined anisotropically.

The theoretical calculations are based on density functional theory (DFT) as implemented in the Vienna *ab initio* simulation package (VASP) [41]. To correctly account for the van der Waals forces, we employed the nonlocal optimized Perdew-Burke-Erznerhof–van der Waals (optPBE-vdW) functionals proposed by Dion *et al.* [42] with parameters by Oyedele *et al.* [27] and Klime *et al.* [43]. Electron correlation effects in the d orbitals of Pd were accounted for in the PBE+U approximation with $U = 4$ eV. To study various compositions of $PdSe_{2-x}Te_x$, we used $2\times2\times1$ supercells, providing nine compositions of $x = \{0, \frac{1}{4}, \frac{1}{2}, \frac{3}{4}, 1, \frac{5}{4}, \frac{3}{2}, \frac{7}{4}, 2\}$. The Brillouin zone was sampled with a Γ-centered Monkhorst-Pack grid of $10\times10\times6$, $6\times12\times10$, and $15\times15\times3$ k points, for the $Pbca$, $C2/c$, and $P\text{-}3m1$ structures, respectively. The electronic wave functions were expanded in a plane-wave basis with a kinetic-energy cutoff of 325 eV. The atomic positions of each composition were optimized until the force on each atom was lower than 10^{-3} eV/Å and the total energy was accurate to 10^{-8} eV. After optimization, the intralayer bond length and interlayer distance were measured. The Gibbs free energy of each structure and composition was calculated using

$$G = E_0 - TS_{\text{vibr}},$$

where E_0 is the ground-state energy calculated from DFT and $E_{\text{vibr}} = TS_{\text{vibr}}$ is the vibrational Gibbs free energy associated with the phonon frequencies ω_i through

$$E_{\text{vibr}} = \sum_i \left\{ \frac{\hbar\omega_i}{2} + k_B T \ln\left[1 - \exp\left(-\frac{\hbar\omega_i}{k_B T}\right)\right]\right\}.$$

The formation energy was calculated as the difference between the Gibbs free energy of the compound and that of the elemental metals, evaluated at $T = 300$ K,

$$G_{\text{form}} = G_{PdSe_{2-x}Te_x} - G_{\text{Pd}} - (2-x)G_{\text{Se}} - xG_{\text{Te}}.$$

We obtain the phonon energies at Γ from density functional perturbation theory (DFPT) calculations in VASP employing unit cells containing $2\times2\times2$ $PdSe_2/Te_2$ unit cells. All optical branches are assumed to be flat and independent of the

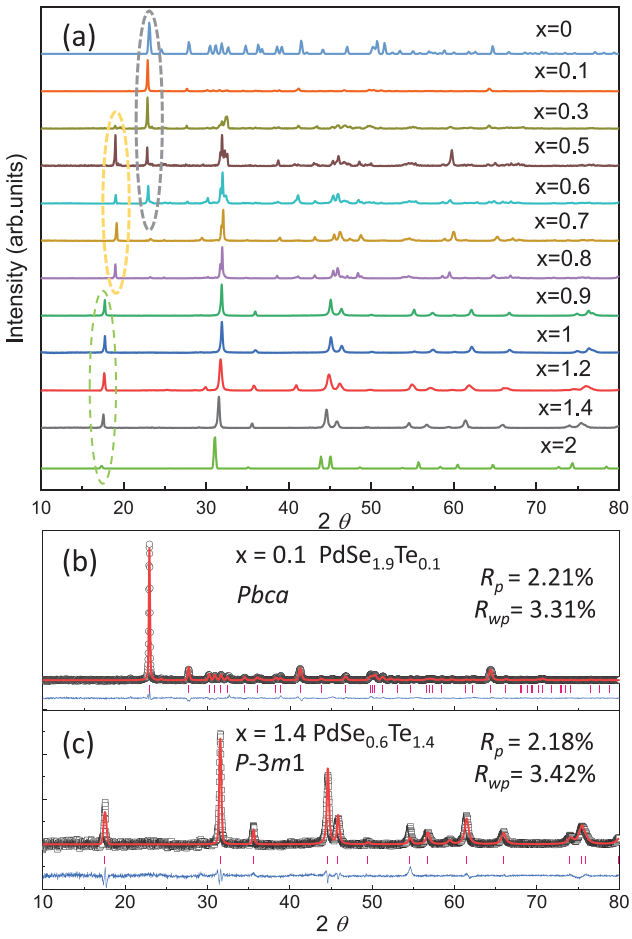

FIG. 2. (a) Powder x-ray diffraction patterns of $PdSe_{2-x}Te_x$ ($0 \leqslant x \leqslant 2$). (b) and (c) Rietveld refinement for (b) $PdSe_{1.9}Te_{0.1}$ and (c) $PdSe_{0.6}Te_{1.4}$. The black circles, red curves, pink bars, and blue curves denote the observed diffraction intensities, the calculated diffraction intensities, the calculated locations of diffraction peaks, and the difference between the calculated and observed diffraction intensities, respectively.

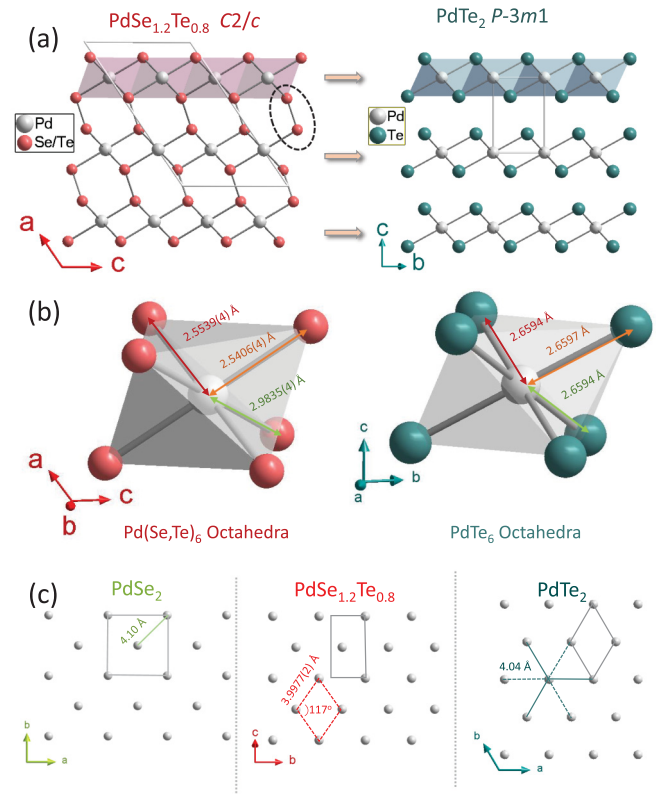

FIG. 3. (a) Ball-and-stick models for $PdSe_{1.2}Te_{0.8}$ with space group $C2/c$ along different directions. (b) Comparison of octahedra in $PdSe_{1.2}Te_{0.8}$ and $PdTe_2$ structures. (c) Metal configurations in Pd planes of $PdSe_2$, $PdSe_{1.2}Te_{0.8}$, and $PdTe_2$.

q vector. The acoustic branches are assumed to have a linear dispersion with a sound velocity given by the first optical phonon energy divided by the smallest reciprocal lattice vector.

Finally, the exfoliation energy of $PdSe_{2-x}Te_x$ was estimated as the difference between the ground-state energies E_0 of the bulk and monolayer forms per unit of surface area.

III. RESULTS

A. Structure evolution

Figure 2(a) shows the x-ray diffraction patterns for $PdSe_{2-x}Te_x$ samples. At first glance, one can clearly observe three different types of structures with one of the corresponding characteristic peaks highlighted in Fig. 2(a). In the Se-rich region $0 \leqslant x \leqslant 0.3$, the XRD peaks shift slightly towards lower angle, as expected with increasing Te content, and the $PdSe_{2-x}Te_x$ maintains the puckered pentagonal $PdSe_2$ structure with orthorhombic lattice. A second phase starts to emerge at $x = 0.3$; although the major phase remains the $PdSe_2$ structure, this new phase becomes more dominant when $x \geqslant 0.5$ and coexists with the $PdSe_2$-type phases until $x = 0.6$. In the composition range of $0.7 \leqslant x \leqslant 0.8$, an XRD pure quality of the new phase was obtained. With further increasee in the Te content for $0.9 \leqslant x \leqslant 2.0$, the structure transforms to the P-3m1(1T) structure. Figures 2(b) and 2(c) are the Rietveld refinement results for the $PdSe_{1.9}Te_{0.1}$ and $PdSe_{0.6}Te_{1.4}$ samples. The refined lattice parameters for $PdSe_{1.9}Te_{0.1}$ are $a = 5.7687(2)$ Å, $b = 5.8973(6)$ Å, $c = 7.7160(8)$ Å, which are slightly bigger than those of $PdSe_2$ ($a = 5.7410$ Å, $b = 5.8660$ Å, $c = 7.6910$ Å) as expected. The refined lattice parameters for the $PdSe_{0.6}Te_{1.4}$ sample are $a = b = 3.9460(9)$ Å and $c = 5.0371(5)$ Å, slightly less than that of CdI_2-type $PdTe_2$ as Se atoms are smaller than Te atoms.

A small crystal from the $PdSe_{1.2}Te_{0.8}$ sample is selected for the x-ray single-crystal diffraction. The determined crystallographic parameters, refinement details, atomic coordinates, occupancies, and equivalent anisotropic displacement parameters are included in Table I (for more crystal structure details, see the Supplemental Material [44]). The refined ratio of Se to Te equals 1.23(2):0.77(2), which is rather close to the nominal composition and consistent with the chemical analysis results from scanning electron microscopy (SEM) analysis. The crystal structure of the refined $PdSe_{1.23(2)}Te_{0.77(2)}$ is shown in Fig. 3(a). The refined $PdSe_{1.23(2)}Te_{0.77(2)}$

TABLE I. Crystallographic data, atomic coordinates, and equivalent isotropic displacement parameters of $PdSe_{1.2}Te_{0.8}$. Here, diff., difference; Occ., occupancy; U_{eq}, Equivalent Isotropic Displacement Parameters; Wyck., Wyckoff position.

	Value
Temperature	295 K
Wavelength	0.71073 Å
Cell parameters	$a = 11.2450(9)$ Å, $b = 4.1877(4)$ Å, $c = 6.8110(5)$ Å, $\beta = 124.326^\circ$, $V = 264.88(4)$ Å^3, $Z = 4$
Space group	$C2/c$ (No. 15)
Absorption coefficient	31.834 mm^{-1}
$F(000)$	511.4
θ range for data collection	4.389–32.921
Reflections collected	2302
Independent reflections	487 ($[R_{int}] = 0.0139$)
Data/restraints/parameters	487/0/18
Goodness of fit on F^2	1.104
Final R indices $[I > 2\sigma(I)]$	$R_1 = 0.0225$, $wR_2 = 0.0623$
R indices (all data)	$R_1 = 0.0228$, $wR_2 = 0.0624$
Largest diff. peak and hole	3.854 and -1.249 e^{-3}

Atom	Wyck.	x	y	z	Occ.	U_{eq} (Å^2)
Pd1	4c	3/4	1/4	1/2	1	0.0120(2)
Se1	8f	0.60958(3)	0.31783(9)	0.05186(5)	0.615(8)	0.0133(2)
Te1	8f	0.60958(3)	0.31783(9)	0.05186(5)	0.385(8)	0.0133(2)

crystallizes in a polymorphic structure in a monoclinic cell with space group $C2/c$ (No. 15), the chalcogen-chalcogen interlayer interactions now appear as covalent bonds, and a three-dimensional framework is visualized in Fig. 3(a). The chalcogen-Pd-chalcogen stacking maintains a similar stacking order with a fundamental building motif of $Pd(Se, Te)_6$ octahedra, just as in the 1T $PdTe_2$ phase. However, the $Pd(Se, Te)_6$ octahedra are much more distorted, and are severely elongated along one direction within the plane, compared with the $PdTe_6$ octahedra in $PdTe_2$ as is shown in Fig. 3(b).

As a result, the chalcogen-chalcogen distance between the adjacent stacking layers decreases down to 2.6338(5) Å in the $PdSe_{1.23(2)}Te_{0.77(2)}$ system from the value of 3.463 Å in the 1T-$PdTe_2$ system, suggesting an effective covalent bonding interaction between the two adjacent layers. Another distinct difference in this Verbeekite polymorphic phase between $PdSe_2$ and $PdTe_2$ is in the Pd metal configurations. As shown in Fig. 3(c), the Pd metals in the Verbeekite polymorphic phase $PdSe_{1.23(2)}Te_{0.77(2)}$ have a rhombus packing with an obtuse angle measuring ∼117°, which is completely different from the rectangular Pd packing (i.e., 90°) in the $PdSe_2$ structure and trigonal antiprismatic Pd packing (i.e., 120°) in the $PdTe_2$ structure. The Pd-Pd distance is ∼3.99 Å, which is smaller than 4.10 Å in the $PdSe_2$ phase and 4.04 Å in the $PdTe_2$ phase.

It is worthwhile to mention that this new polymorphic phase $PdSe_{1.2}Te_{0.8}$ is isostructural with the rare mineral Verbeekite $PdSe_2$ phase. The mineral Verbeekite was discovered naturally in 2002 and synthesized in the laboratory via multianvil high-pressure high-temperature methods at 11.5 GPa and 1300 °C in 2017. On the other hand, a different structural phase transition from orthorhombic to a cubic pyrite-type structure is observed in direct diamond anvil cell studies of $PdSe_2$ crystals under high pressure above 6 GPa without applying the high temperature. $PdSe_{1.2}Te_{0.8}$ has bigger unit cell parameters ($a = 11.2450$ Å, $b = 4.1877$ Å, and $c = 6.8110$ Å) than the high-pressure Verbeekite $PdSe_2$ phase ($a = 8.914$ Å, $b = 4.1542$ Å, and $c = 6.710$ Å) as expected, since the atomic size of Te elements is bigger than that of Se atoms. However, it is rather puzzling why a larger cell of $PdSe_{1.2}Te_{0.8}$ could crystallize in this high-pressure $PdSe_2$ analog Verbeekite-type structure. This unique Se-Se dimer packing structure in the Verbeekite-type $PdSe_{1.2}Te_{0.8}$ phase could potentially offer another promising platform to investigate interesting structural and electrical behaviors near the critical point of two and three dimensionality for TMD materials.

Figure 4 shows the formation energy for $PdSe_{2-x}Te_x$, in the *Pbca* phase, the $C2/c$ phase, and the *P*-3*m*1 phase, calculated using DFT. The theoretical calculations show that the *Pbca* phase is the most stable phase for $x = 0$ ($PdSe_2$); for $x = 0.3$ up to $x = 0.8$, the $C2/c$ phase appears the most stable, and for

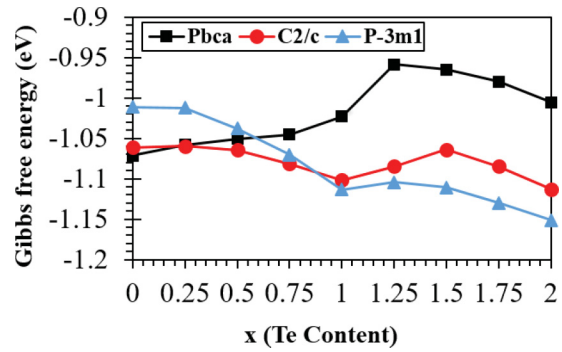

FIG. 4. Formation energy (Gibbs free energy) of *Pbca*, $C2/c$, and *P-3m1* phases of $PdSe_{2-x}Te_x$ at 300 K, calculated using DFT.

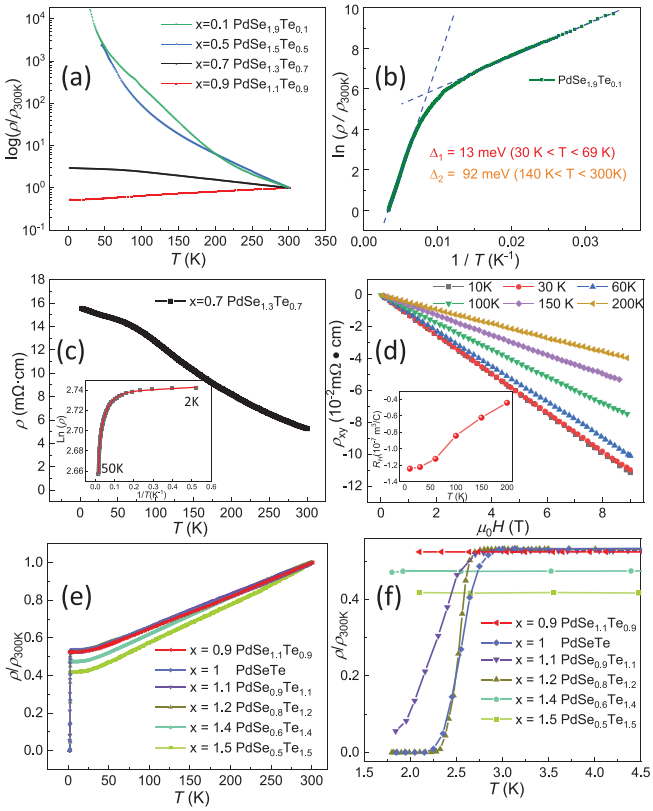

FIG. 5. (a) Temperature dependence of normalized resistivity $(\rho/\rho_{300\,\mathrm{K}})$ in log scale for $PdSe_{2-x}Te_x$ solid solution with $0.1 \leqslant x \leqslant 0.9$. (b) $\ln(\rho/\rho_{300\,\mathrm{K}})$ vs $(1/T)$ for $PdSe_{1.9}Te_{0.1}$. The blue dashed lines represent the fitting using the standard activation model. (c) Electrical resistivity ρ vs temperature T for $PdSe_{1.3}Te_{0.7}$. The inset shows $\ln(\rho)$ vs $(1/T)$ of $PdSe_{1.3}Te_{0.7}$ in the temperature range 2–50 K. The solid red curve is fitted to Eq. (1). (d) Hall resistivity of $PdSe_{1.3}Te_{0.7}$ at 10, 30, 60, 100, 150, and 200 K. The inset shows the evolution of the Hall coefficient R_H with temperature. (e) Temperature-dependent normalized resistance $(R/R_{300\,\mathrm{K}})$ of $PdSe_{2-x}Te_x$ solid solution for $0.9 \leqslant x \leqslant 1.5$. (f) Enlarged view of $R/R_{300\,\mathrm{K}}$ in the low-temperature region 1.8–4.5 K.

$x > 0.8$, the $P\text{-}3m1$ phase has the lowest energy. These results are in excellent agreement with the experimentally grown material, characterized by the x-ray diffraction results shown in Fig. 2. Overall, the agreement is remarkable, although a slight discrepancy between theory and experiment is observed in the $x = 0.3$ to $x = 0.6$ region where experimentally both the *Pbca* and the $C2/c$ phases coexist while our theoretical calculations clearly favor the $C2/c$ phases. We note that the phonon contribution is a significant component of the Gibbs free energy and our theoretical results reveal that the entropy associated with the phonons is an important component in determining which phase is most stable.

B. Electronic properties

Figure 5 shows the changes in electrical transport properties in the $PdSe_{2-x}Te_x$ system upon Te doping. As one can see from Fig. 5(a), a clear crossover in electrical transport accompanied by the semiconductor-to-metal transition

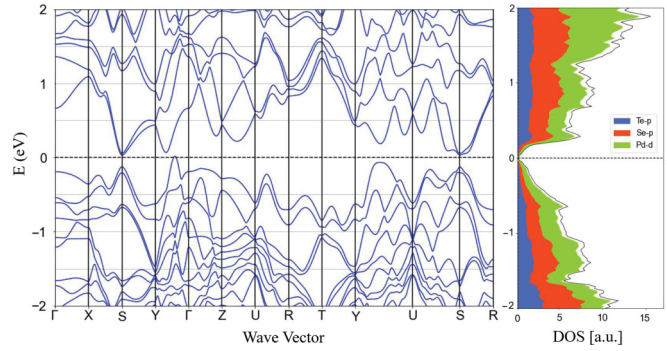

FIG. 6. Band structure and density of states, with the most important orbital contributions indicated, of $PdSe_{1.25}Te_{0.75}$ determined from first principles.

is observed with increasing Te content. Figure 5(b) shows the plot of $\ln(\rho/\rho_{300\mathrm{K}})$ vs $(1/T)$ for a $PdSe_{1.9}Te_{0.1}$ sample, where thermally activated conduction behavior is observed. Two clear linear relations of $\ln(\rho/\rho_{300\mathrm{K}})$ vs. $(1/T)$ are found in the range of 140–300 and 30–69 K, indicating an energy gap of 92 and 13 meV, respectively. Figure 5(c) shows the temperature-dependent electrical resistivity $\rho(T)$ for the Verbeekite polymorphic phase of $PdSe_{1.3}Te_{0.7}$. The resistivity value is weakly dependent on the temperature and shows an overall semiconducting behavior from room temperature down to 50 K. An anomalous kink arises at the temperature ~50 K, and a clear change in the slope of resistivity is observed afterwards. The resistivity increases more gently and has a tendency of saturation below 50 K, which may be related to the weak localizations of electrons caused by the disorders in this system.

The semiconducting behavior of the Verbeekite phase is also verified with theoretical DFT calculations. Figure 6 shows the calculated band structure and density of states (DOS) of $PdSe_{1.25}Te_{0.75}$. The DFT results show a small (15 meV) indirect band gap for the $C2/c$ phase in agreement with the experimental transport measurements. The conduction band minimum appears at the S point, while the valence band maximum appears along the Γ-Y line. We note that we chose a Hubbard U of 4 eV for all our calculations. To verify whether this is a physically realistic choice, we determined the Hubbard U using linear response theory and found values of 3.1, 2.9, and 2.7 eV for the $P3m1$, $C2c$, and *Pbca* phases of $PdSe_2$. This indicates that our Hubbard U may be slightly overestimated although the linear response is known to underestimate the Hubbard U. Finally, the difference in Hubbard U between the three phases indicates that follow-up theoretical work should consider the impact of different U values for different phases and compositions.

The inset of Fig. 5(c) highlights the plot of $\ln\rho$ vs $(1/T)$ below 50 K. The curves become almost T independent at low temperature between 2 and 30 K, indicating the existence of a hopping process in the materials. Several general hopping models could contribute to the electrical transport in $PdSe_{2-x}Te_x$. One is the nearest-neighbor-hopping (NNH) model, where ρ is proportional to $\exp(E_A/k_BT)$. Here, E_A is the activation energy, and k_B is the Boltzmann constant [45]. Another model describes variable-range hopping (VRH),

where $\rho \propto \exp[T_0/T]^{1/(1+d)}$ and which often occurs between states with larger spatial distance but closer energy [46]. Here, T_0 is a characteristic temperature, and d is the dimensionality of the solid-state materials. VRH has been found in many disordered systems [47–49].

In our system, one can clearly observe that the slope decreases continuously with decreasing temperature, which suggests the existence of multiple conducting channels. Therefore we utilized one NNH model together with one VRH model to fit our low-temperature resistivity data below 50 K using the following equation:

$$R(T)^{-1} = R_0^{-1} + R_1^{-1}\exp[-E_1/2k_BT] + R_2^{-1}\exp[-(T_2/T)^{\frac{1}{3}}], \quad (1)$$

where E_1 is the activation energy, T_2 is the characteristic temperature, and R_0, R_1, and R_2 are the related resistance coefficients. Here, the temperature-independent R_0^{-1} represents the scattering of electrons by disorders in low temperature and is extracted to be 0.0647. The extracted activation energy E_1 is about 2 meV. The low activation energy E_1 reveals inhomogeneous localization distributions in this system, and the nearly free carriers are weakly localized by the disorder. When the temperature decreases below 30 K, the VRH dominates, and the characteristic temperature T_2 is extracted to be $\sim 4.8\times10^4$ K. Here, the characteristic temperature has a positive relation to the optimal hopping distance of the localized electrons, and the yielding value is consistent with that of many other TMD materials [49]. The coefficients R_1^{-1} and R_2^{-1} are extracted to be 0.004 and 19, respectively. We have also tried to fit out data with one-dimensional (1D), 2D, and 3D VRH models, and all of them fail to converge. When combining one NNH with a VRH model of 1D and 3D, no convergence on the fit is observed either. The fact that only the 2D VRH combined with the NNH model fits the data well, suggests that the structure of this new Verbeekite polymorphic phase is closer to quasi-2D rather than 3D.

Figure 5(d) shows the temperature dependence of the Hall resistivity ρ_{xy} for $PdSe_{1.3}Te_{0.7}$, exhibiting the new $C2/c$ phase, at 10, 30, 60, 100, 150, and 200 K. Here, ρ_{xy} shows linearly dependent behaviors with the magnetic field. The slopes are all negative, indicating that the charge carriers are dominantly electrons near the Fermi surface. The Hall coefficient $R_H = \rho_{xy}/\mu_0 H$, estimated by the linearly fitting of ρ_{xy}, is shown in the inset of Fig. 4(d). R_H scales almost monotonically with temperature, and there are no significant changes in R_H around 50 K. The charge-carrier density from single band approximation is estimated to be 5.12×10^{19} cm^{-3} at 10 K, which is about two orders smaller than the 5.5×10^{21} cm^{-3} extracted for $PdTe_2$ in Ref. [50].

Finally, Figs. 5(e) and 5(f) show the temperature dependence of the in-plane resistivity ratio $\rho/\rho_{300\,\mathrm{K}}$ of $PdSe_{2-x}Te_x$ samples with x in the range $0.9 \leqslant x \leqslant 1.5$. All of these samples show metallic behavior with residual resistivity ratios (RRRs) around 2, which are smaller than the RRR of 75 of the $PdTe_2$ single crystal [50], reflecting the substantial disorder induced by Te substitution. Remarkably, in the composition range $1.0 \leqslant x \leqslant 1.2$, superconductivity suddenly occurs with an onset T_c close to 2.7 K. For compositions beyond $x > 1.2$, no superconductivity is detected above 1.8 K (the limit of our instrument), but the samples could possibly still be superconducting below 1.8 K, as 1T-$PdTe_2$ is superconducting at 1.65 K.

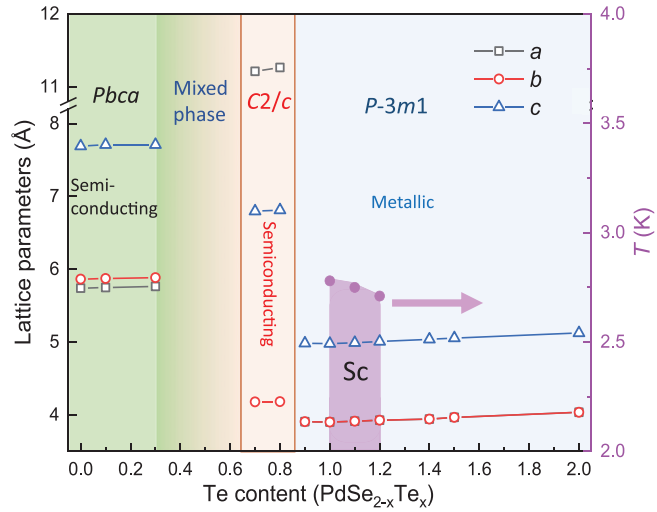

FIG. 7. Phase diagram of $PdSe_{2-x}Te_x$ vs Te content x. Sc, superconducting phase. Open squares, circles, and triangles show the lattice parameters a, b, and c respectively. Solid purple balls show the onset superconducting transition temperature determined from transport measurements.

C. Phase diagram

Figure 7 summarizes the rich phase diagram for the $PdSe_{2-x}Te_x$ system, where both crystal symmetry and lattice parameters are listed. With increasing Te content x, the structure of $PdSe_{2-x}Te_x$ retains an orthorhombic phase up to $x = 0.3$. The new Verbeekite-type polymorphic phase starts to emerge when $x \geqslant 0.3$ and remains stable up to $x = 0.8$. With further doping beyond $x = 0.9$, the monoclinic phase becomes unstable, and the samples transform to a P-3m1 (1T) phase. Within a narrow region of P-3m1 (1T) phase when $1.0 \leqslant x \leqslant 1.2$, the samples show superconductivity with onset at T_c close to 2.7 K, as reported by us previously [37].

IV. CONCLUSION

In conclusion, we have carried out a systematic study of isoelectronic substitution of Te for Se in $PdSe_{2-x}Te_x$ solid solutions. A structural evolution with increasing Te fraction from the *Pbca* $PdSe_2$ phase to the P-3m1 $PdTe_2$ phase was observed accompanied with clearly distinct electrical transport behavior. A new Verbeekite-type polymorphic $C2/c$ structure was discovered within a narrow range of Te composition ($x = 0.3$ to $x = 0.8$), and the $C2/c$ structure has a distinct packing structure which is different from all known TMDs to date. Theoretical first-principles calculations agree with the experimental findings and revealed that the phonon contribution to the free energy is an important factor in making *Pbca* and $C2/c$ favorable phases. The $C2/c$ phase showed electron-dominated charge carriers and displayed an unusual electrical conductivity behavior which could be well explained through the combined nearest-range-hopping and variable-range-hopping model. In the P-3m1 (1T) phase region, an enhanced superconductivity emerges in a narrow range with onset at T_c of about 2.7 K. The rich phase

diagram and very rare polymorphic structure discovered in this system could provide a new material platform to further investigate transport and electronic properties of different types of polymorphs in the TMD structure that are of significant interest.

ACKNOWLEDGMENTS

This work at University of Texas at Dallas is supported by U.S. Air Force Office of Scientific Research Grant No. FA9550-19-1-0037 and the National Science Foundation (Grant No. DMR-1921581). We also acknowledge the support from the Office of Research at University of Texas at Dallas through the Seed Program for Interdisciplinary Research (SPIRe) and the Core Facility Voucher Program. The project or effort depicted is sponsored by the Department of Defense, Defense Threat Reduction Agency. The content of the information does not necessarily reflect the position or the policy of the federal government, and no official endorsement should be inferred.

[1] G. Fiori, F. Bonaccorso, G. Iannaccone, T. Palacios, D. Neumaier, A. Seabaugh, S. K. Banerjee, and L. Colombo, Nat. Nanotechnol. **9**, 768 (2014).
[2] K. S. Novoselov, A. Mishchenko, A. Carvalho, and A. H. Castro Neto, Science **353**, aac9439 (2016).
[3] Q. Yun, L. Li, Z. Hu, Q. Lu, B. Chen, and H. Zhang, Adv. Mater. **32**, 1903826 (2020).
[4] Q. H. Wang, K. Kalantar-Zadeh, A. Kis, J. N. Coleman, and M. S. Strano, Nat. Nanotechnol. **7**, 699 (2012).
[5] W. Choi, N. Choudhary, G. H. Han, J. Park, D. Akinwande, and Y. H. Lee, Mater. Today **20**, 116 (2017).
[6] Y. Zhang, Y. Iwasa, J. Miyazaki, W. Shi, N. Inoue, J. Ye, M. Yoshida, R. Suzuki, and Y. Saito, Sci. Rep. **5**, 12534 (2015).
[7] A. Ciarrocchi, A. Avsar, D. Ovchinnikov, and A. Kis, Nat. Commun. **9**, 919 (2018).
[8] J. Li, X. Yang, Y. Liu, B. Huang, R. Wu, Z. Zhang, B. Zhao, H. Ma, W. Dang, Z. Wei, K. Wang, Z. Lin, X. Yan, M. Sun, B. Li, X. Pan, J. Luo, G. Zhang, Y. Liu, Y. Huang *et al.*, Nature (London) **579**, 368 (2020).
[9] S. Wu, V. Fatemi, Q. D. Gibson, K. Watanabe, T. Taniguchi, R. J. Cava, and P. Jarillo-Herrero, Science **359**, 76 (2018).
[10] M. Chhowalla, H. S. Shin, G. Eda, L. J. Li, K. P. Loh, and H. Zhang, Nat. Chem. **5**, 263 (2013).
[11] C. Jin, E. C. Regan, A. Yan, M. Iqbal Bakti Utama, D. Wang, S. Zhao, Y. Qin, S. Yang, Z. Zheng, S. Shi, K. Watanabe, T. Taniguchi, S. Tongay, A. Zettl, and F. Wang, Nature (London) **567**, 76 (2019).
[12] S. Ulstrup, R. J. Koch, S. Singh, K. M. McCreary, B. T. Jonker, J. T. Robinson, C. Jozwiak, E. Rotenberg, A. Bostwick, J. Katoch, and J. A. Miwa, Sci. Adv. **6**, eaay6104 (2020).
[13] L. Wang, E. M. Shih, A. Ghiotto, L. Xian, D. A. Rhodes, C. Tan, M. Claassen, D. M. Kennes, Y. Bai, B. Kim, K. Watanabe, T. Taniguchi, X. Zhu, J. Hone, A. Rubio, A. N. Pasupathy, and C. R. Dean, Nat. Mater. **19**, 861 (2020).
[14] Q. Li, C. He, Y. Wang, E. Liu, M. Wang, Y. Wang, J. Zeng, Z. Ma, T. Cao, C. Yi, N. Wang, K. Watanabe, T. Taniguchi, L. Shao, Y. Shi, X. Chen, S. J. Liang, Q. H. Wang, and F. Miao, Nano Lett. **18**, 7962 (2018).
[15] H. X. Zhong, S. Gao, J. J. Shi, and L. Yang, Phys. Rev. B **92**, 115438 (2015).
[16] B. E. Brown, Acta Cryst. **20**, 264 (1966).
[17] Y. Deng, Y. Lai, X. Zhao, X. Wang, C. Zhu, K. Huang, C. Zhu, J. Zhou, Q. Zeng, R. Duan, Q. Fu, L. Kang, Y. Liu, S. J. Pennycook, X. R. Wang, and Z. Liu, J. Am. Chem. Soc. **142**, 2948 (2020).
[18] E. Bjerkelund and A. Kjkshus, Acta. Chem. Scand. **21**, 513 (1965).
[19] B. Yan and C. Felser, Annu. Rev. Condens. Matter Phys. **8**, 337 (2017).
[20] T. A. Empante, Y. Zhou, V. Klee, A. E. Nguyen, I. H. Lu, M. D. Valentin, S. A. Naghibi Alvillar, E. Preciado, A. J. Berges, C. S. Merida, M. Gomez, S. Bobek, M. Isarraraz, E. J. Reed, and L. Bartels, ACS Nano **11**, 900 (2017).
[21] R. Sankar, G. Narsinga Rao, I. P. Muthuselvam, C. Butler, N. Kumar, G. Senthil Murugan, C. Shekhar, T. R. Chang, C. Y. Wen, C. W. Chen, W. L. Lee, M. T. Lin, H. T. Jeng, C. Felser, and F. C. Chou, Chem. Mater. **29**, 699 (2017).
[22] J. Jiang, Z. K. Liu, Y. Sun, H. F. Yang, C. R. Rajamathi, Y. P. Qi, L. X. Yang, C. Chen, H. Peng, C. C. Hwang, S. Z. Sun, S. K. Mo, I. Vobornik, J. Fujii, S. S. P. Parkin, C. Felser, B. H. Yan, and Y. L. Chen, Nat. Commun. **8**, 13973 (2017).
[23] H. Luo, W. Xie, J. Tao, H. Inouec, A. Gyenis, J. W. Krizan, A. Yazdani, Y. Zhu, and R. J. Cava, Proc. Natl. Acad. Sci. USA **112**, E1174 (2015).
[24] F. Gronvold and E. Rost, Acta Chem. Scand. **10**, 1620 (1956).
[25] F. Hulliger, J. Phys. Chem. Solids **26**, 639 (1965).
[26] R. Kempt, A. Kuc, and T. Heines, Angew. Chem., Int. Ed. **59**, 9242 (2020).
[27] A. D. Oyedele, S. Yang, L. Liang, A. A. Puretzky, K. Wang, J. Zhang, P. Yu, P. R. Pudasaini, A. W. Ghosh, Z. Liu, C. M. Rouleau, B. G. Sumpter, M. F. Chisholm, W. Zhou, P. D. Rack, D. B. Geohegan, and K. Xiao, J. Am. Chem. Soc. **139**, 14090 (2017).
[28] Y. Yu, F. Yang, X. F. Lu, Y. J. Yan, Y. H. Cho, L. Ma, X. Niu, S. Kim, Y. W. Son, D. Feng, S. Li, S. W. Cheong, X. H. Chen, and Y. Zhang, Nat. Nanotechnol. **10**, 270 (2015).
[29] Y. Ma, L. Kou, X. Li, Y. Dai, and T. Heine, NPG Asia Mater. **8**, e264 (2016).
[30] Q. Liang, Q. Wang, Q. Zhang, J. Wei, S. X. Lim, R. Zhu, J. Hu, W. Wei, C. Lee, C. Sow, and W. Zhang, Adv. Mater. **31**, 1807609 (2019).
[31] W. L. Chow, P. Yu, F. Liu, J. Hong, X. Wang, Q. Zeng, C. H. Hsu, C. Zhu, J. Zhou, X. Wang, J. Xia, J. Yan, Y. Chen, D. Wu, T. Yu, Z. Shen, H. Lin, C. Jin, B. K. Tay, and Z. Liu, Adv. Mater. **29**, 1602969 (2017).
[32] G. Zhang, M. Amani, A. Chaturvedi, C. Tan, J. Bullock, X. Song, H. Kim, D. H. Lien, M. C. Scott, H. Zhang, and A. Javey, Appl. Phys. Lett. **114**, 253102 (2019).

[33] M. A. Elghazali, P. G. Naumov, H. Mirhosseini, V. S. L. Mchler, W. Schnelle, C. Felser, and S. A. Medvedev, Phys. Rev. B **96**, 060509(R) (2017).
[34] W. Zheng, R. Schönemann, N. Aryal, Q. Zhou, D. Rhodes, Y. C. Chiu, K. W. Chen, E. Kampert, T. Förster, T. J. Martin, G. T. McCandless, J. Y. Chan, E. Manousakis, and L. Balicas, Phys. Rev. B **97**, 235154 (2018).
[35] F. Fei, X. Bo, R. Wang, B. Wu, J. Jiang, D. Fu, M. Gao, H. Zheng, Y. Chen, X. Wang, H. Bu, F. Song, X. Wan, B. Wang, and G. Wang, Phys. Rev. B **96**, 041201(R) (2017).
[36] H. Leng, C. Paulsen, Y. K. Huang, and A. de Visser, Phys. Rev. B **96**, 220506(R) (2017).
[37] W. Liu, S. Li, H. Wu, N. Dhale, P. Koirala, and B. Lv, Phys. Rev. Mater. **5**, 014802 (2021).
[38] A. C. Roberts, W. H. Paar, M. A. Cooper, D. Topa, A. J. Criddle, and J. J. Verbeekite, Mineral. Mag. **66**, 173 (2002).
[39] E. Selb, M. Tribus, and G. Heymann, Inorg. Chem. **56**, 5885 (2017).
[40] B. H. Toby and R. B. Von Dreele, J. Appl. Cryst. **46**, 544 (2013).
[41] G. Kresse and J. Furthmüller, Phys. Rev. B **54**, 11169 (1996).
[42] M. Dion, H. Rydberg, E. Schröder, D. C. Langreth, and B. I. Lundqvist, Phys. Rev. Lett. **92**, 246401 (2004).
[43] J. Klime, D. R. Bowler, and A. Michaelides, J. Phys.: Condens. Matter **22**, 022201 (2010).
[44] See Supplemental Material at http://link.aps.org/supplemental/10.1103/PhysRevB.104.024507 for crystal structure details of the Verbeekite $PdSe_{1.2}Te_{0.8}$.
[45] V. F. Gantmakher, *Electrons and Disorder in Solids* (Oxford University Press, Oxford, 2005).
[46] N. F. Mott and E. A. Davis, *Electronic Processes in Non-Crystalline Materials* (Oxford University Press, Oxford, 2012).
[47] Z. G. Yu and X. Song, Phys. Rev. Lett. **86**, 6018 (2001).
[48] M. Y. Han, J. C. Brant, and P. Kim, Phys. Rev. Lett. **104**, 056801 (2010).
[49] H. Qiu, T. Xu, Z. Wang, W. Ren, H. Nan, Z. Ni, Q. Chen, S. Yuan, F. Miao, F. Song, G. Long, Y. Shi, L. Sun, J. Wang, and X. Wang, Nat. Commun. **4**, 2642 (2013).
[50] Amit and Y. Singh, Phys. Rev. B **97**, 054515 (2018).